DISTORTION CORRECTION IN MAGNETIC RESONANCE IMAGING USING THE SIMULATED POINT SPREAD FUNCTION

BY

GENEVIEVE M. LABELLE

THESIS

Submitted in partial fulfillment of the requirements
for the degree of Master of Science in Electrical and Computer Engineering
in the Graduate College of the
University of Illinois at Urbana-Champaign, 2016

Urbana, Illinois

Adviser:

Associate Professor Brad Sutton

ABSTRACT

Geometric distortion is a highly prevalent issue for echo-planar imaging (EPI), due to long readout times and field inhomogeneity. Previously, the measured point spread function (PSF) has been shown to be effective in correcting this distortion. In this work, we reconstruct an image quickly and address the distortion with a point spread function that was generated entirely through simulation using the trajectory and measured field map. The distortion correction with this approach is shown to be better than k-space based iterative reconstructions and is robust to high differentials in magnetic field maps when we use an optimal trajectory. In addition, this technique is well-suited to parallel implementation, as the system matrix used is sparse.

To my mother, for her fierce love and stubborn confidence in me.
To my father, our Guardian, for his love of learning and for being a model of hard work and dedication.
To Caroline, Aden, and Carter, may we find strength sola fide.

ACKNOWLEDGMENTS

Thank you to Dr. Brad Sutton for his guidance and support over the years. Thank you as well to Dr. Wen-Mei Hwu for his wisdom and encouragement and to Marie-Pierre Lassiva-Moulin for her kindness and support. I would also like to acknowledge the National Science Foundation (NSF) Graduate Research Fellowship Program, the NSF NeuroEngineering Integrative Graduate Education and Research Traineeship, and the Nadine Barrie Smith Memorial Fellowship for support of this thesis work. Thank you to Joe Holtrop, Giang-Chau Ngo, Alex Cerjanic, and Aaron Anderson for lending their eyes and their brains to the development of this work. Thank you to my family, for their love and for providing positive distractions. Thank you to Katie Amidon, Kristin Amenson, Tim Schowalter, Allison DiLiberto, and Julia LaBelle, for being my sisters and brother. Thank you to Joel Amidon for sharing his academic wisdom. Thank you to Julia LaBelle, for all of the puppy pics. Thank you to Krista Evensen, for the backrubs. Thank you to Kristin Duffy, for the highly effective scrum sessions. Thank you to Marcia Mifflin, for the laughter and wine and for years of chicken salad and jello, and to Uncle Mark, for cheese and crackers. Thank you to Aunt Linda and the Evensens for taking me to Michigan and empowering me to finish one more year! Thank you to Aunt Colette, my personal chocolate supplier. Thank you to Eugene, for hitting up late night study spots with in me in the final weeks. Thank you to Adrian, for hosting the wine and cheese nights.

TABLE OF CONTENTS

LIST OF FIGURES

LIST OF ABBREVIATIONS

SPSF	Simulated Point Spread Function
BWPP	Bandwidth Per Pixel
MRI	Magnetic Resonance Imaging
fMRI	Functional Magnetic Resonance Imaging
NRMSE	Norm Root Mean Square Error
GPU	Graphics Processing Unit

CHAPTER 1

INTRODUCTION

Magnetic resonance imaging (MRI) is widely used in medicine and research to capture brain structure and function in vivo. Functional MRI (fMRI) is a specific application of MRI used to represent the changes in brain activity in a time sequence of images. Two domains in which time presents challenges for fMRI: in data acquisition and in image reconstruction.

1.1 Data Acquisition and Temporal Resolution

Time plays a critical role in acquisition, as fMRI resolution is both spatial and temporal. MRI in general is analogous to photography, in that image quality can be quantified by the two-dimensional spatial resolution, or the sharpness of an image. In this sense, fMRI, a time sequence of MRIs, is comparable to video, a time sequence of photographs, where time is the third dimension, and quality is measured in temporal resolution (time delta between sequential images). High temporal resolution is critical for measuring rapidly changing brain states. fMRI is only possible due to superfast imaging techniques such as echo-planar imaging (EPI). In order to decrease the time between images to achieve a more continuous time sequence, imagers must reduce the acquisition time for each image.

Unfortunately, in order to achieve shorter acquisition times, one must sacrifice image quality. This trade-off is highly prevalent in areas of the brain near air-tissue interfaces, such as behind the nasal cavities, where resulting images are highly distorted. Affected areas include the hippocampus, a memory center, and the amygdala, which processes emotion. This limits the quality of fMRI images for research done in memory processing. Such research is critical to understanding pathology of neurodegenerative diseases, such as Alzheimer's disease. This work will primarily focus on compensating

for the resulting image artifacts.

1.2 Reconstruction Speed

Additionally, time plays an important role in the reconstruction stage of fMRI, since cost of reconstruction escalates quickly for the many time sequence images. For images acquired on Cartesian grids, we can navigate this challenge by using the fast Fourier transform (FFT), an algorithm designed for efficiency. However, the FFT cannot be applied to data acquired on non-Cartesian grids; other algorithms, such as gridding data to a Cartesian grid, must be employed.

One way to save time in reconstruction, just as in any domain, is to perform computations in parallel, rather than sequentially. Consider image reconstruction in terms of a large pile of laundry: either one can do one load at a time at one machine, or one can complete the task in a fraction of the time by doing multiple loads at once at a laundromat. There has been a significant amount of work done in order to parallelize these reconstructions using a graphics processing unit (GPU), which work well for a given problem size. Unfortunately, the problem size that these algorithms can handle is limited by GPU memory. Therefore, the field needs more algorithms which are scalable, meaning they can continue to be used for larger and larger problem sizes.

This work addresses two issues: (1) distortion caused by accelerated data acquisition and (2) memory constraints for parallel reconstruction. We introduce a method that combines novel acquisition and reconstruction techniques to better correct for image distortion, which relies upon a highly sparse system matrix for a more scalable algorithm for application on a GPU.

CHAPTER 2

BACKGROUND AND THEORY

2.1 Magnetic Resonance Imaging

Magnetic resonance imaging (MRI) relies on the properties of protons in a magnetic field. In a large magnetic field, a significant portion of the protons will align with the field, which we will refer to here as the B-field. In MRI, the protons in the imaged tissue are pushed out of alignment with the B-field by a radio-frequency (RF) pulse. The signal generated then depends on the frequency of precession of the excited protons about the axis of the B-field. Magnetic gradients change the magnetic field that the protons experience and change the protons' rate of precession, and MRI uses this property for spatial localization of the signal.

Thus, uniformity of the magnetic field is critical to signal localization; a proton experiencing a different magnetic field will precess at a different frequency, accumulate a different amount of phase, and its signal will then be mapped to the wrong spatial position. Geometric image distortion is the image artifact resulting from mismapping the spatial position of the signal.

2.2 Sources of Field Inhomogeneity

2.2.1 Magnetic Susceptibility

The sources of field inhomogeneity most relevant to this work are due to the effects of magnetic susceptibility. Magnetic susceptibility is the property relating how a material is magnetized by an applied magnetic field. The effects of magnetic susceptibility present both benefits and challenges in MRI.

Susceptibility can be used to provide contrast in images; fMRI leverages

the blood-oxygenation-level dependent (BOLD) contrast, measuring where oxygenated blood flows into when a particular part of the brain is active during a task. BOLD-contrast is a result of the difference in susceptibility of oxygenated and deoxygenated blood in the brain.

However, large differences in susceptibility within a region cause major artifacts in the resulting image, including distortions of more than a centimeter [1]. Specifically, distortion due to susceptibility differences is highest in the brain at air-tissue interfaces, such as near the sinuses.

These effects are highly relevant for single-shot fast imaging methods with long readouts of data as a large portion of k-space is sampled. Single shot imaging is used in fMRI in order to sample the entire image quickly to get many repeats of the imaging across time to see how signal changes are correlated with tasks. Longer readout times lead to greater accumulation of phase between lines in the phase-encode direction, causing geometric distortion [2]. These effects are exacerbated by stronger magnetic fields, as small differences in field strength lead to larger differences in Larmor frequency in higher fields.

2.2.2 Other Causes of Field Inhomogeneity

Various physical phenomena can contribute to non-uniformity of the magnetic field. Careful shimming is necessary to make the static magnetic field as homogeneous as possible, but variations in magnetic field strength will persist [3]. Chemical shift effects are a result of the different chemical environments of the imaged spins and are manifested as a shift in the resonance frequency of the spins. Fat protons, for example, are not decoded properly in MRI if the chemical shift effect is not accounted for, as a shift in the resonance frequency leads to a shift of its interpreted location in the frequency-encode direction. Fortunately, this effect is easily compensated for with fat suppression methods in scan, minimizing the signal produced by the shifted elements [4]. Eddy current effects result in minor artifacts in images as well, but these are largely negligible in acquisitions on modern hardware that have precompensation software [5].

2.3 Distortion and Signal Decay in MRI

We will consider two types of distortion artifacts: geometric distortion due to field inhomogeneity and intensity distortion due to signal loss.

2.3.1 Geometric Distortion and the Signal Equation

In order to quantify the effect of the field inhomogeneity and translate it into an understanding of the geometric distortion, we use the following equation for the signal S as a function of the value of the field map ΔB at each acquired point in k-space:

$$S(m\Delta k_x, n\Delta k_y) = \int\int \rho(x,y) e^{-(nT \pm m\Delta t + TE)/T_2} e^{i\gamma \Delta B(nT \pm m\Delta t)} e^{i(m\Delta k_x x + n\Delta k_y y)} dxdy \tag{2.1}$$

where TE is the echo time, n is the nth line in the phase-encode direction (k_y), m is the mth point in the readout direction (k_x), Δt is the dwell time on each point, T is the time interval between adjacent phase-encode lines, and ΔB is the field inhomogeneity.

We can then transform that equation to see how the resulting image is a function of the correct image, with pixel shifts proportional to the off-resonance of the field at a given location (x, y) for a Cartesian trajectory [6].

$$\tilde{\rho}(x,y) = \rho(x \pm \frac{\Delta B(x,y)}{G_x}, y \pm \frac{\Delta B(x,y)}{\bar{G}_y \tau}) \tag{2.2}$$

Similarly, radial blurring is observed in spiral imaging, as the center of k-space is sampled first and sampling continues out from the center.

2.3.2 Intensity Distortion due to Signal Decay

On the other hand, intensity distortion due to the accelerated signal decay in the images is a consequence of in-voxel dephasing of spins. Consider NASCAR racecars doing many laps along a large track. At the beginning of the race, the cars are very close to one another (in phase) but travel at slightly different speeds. The utility of a long course is to separate the cars in order to discern the fastest; after many laps, the cars will be spread out

around the track (out of phase). If the magnetic field that neighboring protons experience is not homogeneous, the protons precess at slightly different frequencies. Once again, this effect is more prevalent for images with long echo times. After a long period of time, the protons precessing at different rates within a voxel move out of phase. Since phase coherence is necessary to generate a signal, the signal is lost for that voxel [2].

2.3.3 Bandwidth Per Pixel

In order to describe the spatial shift in the image caused by a given off-resonance component, we use a measure called bandwidth per pixel (BWPP), where bandwidth is the inverse of the time spent going from one sample to the next. This is inherently high in the frequency-encode direction, as neighboring pixels are acquired one after another. With a high BWPP, the distortion will result in very small shifts. In the phase encode direction the BWPP will be much smaller and distortions will be higher. $BWPP$ in the phase-encode direction is defined as the inverse of the echospacing divided by the number of lines sampled in the phase-encode direction. Taking advantage of parallel imaging by using a multiple receiver channel coil in order to reduce the sampling requirement by a factor of R, an $N \times N$ sized EPI requires N/R evenly spaced acquisition lines, leading to a much lower BWPP. Typically, R is equal to 2 or 3 for receiver coils that have up to 32 channels.

$$BWPP = \frac{1}{echospacing} \times \frac{1}{N} \times R \tag{2.3}$$

One can then determine the size of the distortion (in terms of pixels) resulting from the field map at location (x,y) using the following, assuming that both the FM and the BWPP are given with units of Hz and Hz/pixel:

$$\delta = \frac{FM(x,y)}{BWPP} \tag{2.4}$$

This reinforces the observation that distortion due to field inhomogeneity is greater in the phase-encode direction, where BWPP is lower, than in the frequency-encode direction. In terms of bandwidth per pixel, it is easy to see how the acquisition trajectory, timing, and field map all play into the degree of distortion in an image [5].

2.4 Point Spread Functions and Field Maps

Before discussing the various methods used to correct for the artifacts of field inhomogeneity, we will define two useful tools for describing the field and its effects on an image.

2.4.1 Point Spread Function

The first tool to note is the point spread function (PSF), which describes the blur and geometric shift of a given point in image space. Liang describes the observed image as a convolution of the object with the point spread function [4]:

$$\hat{I}(x) = I(x) * h(x) \tag{2.5}$$

Robson et al. measure the spatially-varying PSF of each pixel in constant time by preceding each line measurement with phase-encoding prewinder gradients of equal length that scale in height, though the multiple reference measurements are needed [6].

2.4.2 Field Map

Another critical tool for field correction is the field map. Field maps are measured using two or more measurements of the image with different echo times offset by some constant increment. When the phase differences between the images are fitted to a line, the rate of phase accumulation is used as the field map. This is shown in the following equation [2]:

$$\Delta B = \frac{\angle I_{TE+\Delta t} - \angle I_{TE}}{\Delta t} \tag{2.6}$$

The field map can be modeled with the distorted image to create a new signal, which can be transformed back to the corrected image. Additionally, the field map can be included in inverse-problem approaches to reconstructing field-map-corrected images [7].

2.4.3 Trade-Offs

These two tools bring different benefits and limitations to field correction for MRI. Zeng and Constable explore the trade-offs of the two and methods that employ them in [8]. They conclude that while the field map is susceptible to the effects of phase wrap, partial volume effects, and eddy currents, it can be used to account for phase-encode and readout distortions. Contrary to Zeng's conclusion, Sutton et al. find that the field map can also account for intensity distortions due to in-voxel dephasing [9]. The PSF, on the other hand, is immune to the aforementioned effects and can also provide intensity and phase-encode geometric distortion information for the same measurement time. If distortion correction in the readout direction is also desired, longer acquisitions would be needed to differentially encode the PSF in that direction. However, these distortions in the readout direction are usually negligible and can be ignored in EPI imaging.

CHAPTER 3

REVIEW OF LITERATURE

3.1 Image Correction Methods

Field inhomogeneity distortions in EPI are well understood, and there are several techniques for field correction that are specific to EPI.

3.1.1 Conjugate Phase Reconstruction

A conjugate phase reconstruction uses the field map and timing vector to compensate for the phase accumulation due to the field inhomogeneity and can be easily applied to non-Cartesian acquisitions. The signal is multiplied by the conjugate of the product of time and the field map, canceling the accumulated phase.

$$\hat{f}(\vec{r}) = \sum_{l} S(\vec{k_l}) e^{i2\pi\Delta B(\vec{r})t_l} e^{i2\pi\vec{k_l}\vec{r}} \tag{3.1}$$

where $\vec{r}$ is the position in image space, $S(\vec{k})$ is the signal at k-space location $\vec{k}$, $\Delta B(\vec{r})$ is the measured field map at $\vec{r}$, and t is the acquisition time of the sample at $\vec{k}$. Noll proposes a time-segmented approach in [10] so that fast, gridding reconstruction can be used for non-Cartesian acquisitions. There, the time segmentation allows approximation of the field for a given time block, so that phase correction can be applied after gridding without dependence on the exact spatial position or acquisition time.

3.1.2 Pixel Shifting

Field maps have long been used to directly design pixel-shift maps for correction of field effects for the Cartesian acquisition in EPI [5, 11, 12, 13]. How-

ever, much has also been done for EPI without knowledge of the field map by simply adapting the acquisition; manipulation of the encoding scheme in turn manipulates the distortion. This eliminates the need for a long field map acquisition and may make the technique more adaptable to dynamic field inhomogeneity correction.

Chang's rectification method in [14] acquires two images using different gradients and post-processes the images in order to achieve a rectified image. Morgan expands on this method using non-linear interpolation to compute the distortion from the magnitude images [15]. This method is more susceptible to low SNR effects and largely is competitive with other correction methods, but does depend on heavy post-processing, including boundary matching and integration [1].

Phase-labeling for additional coordinate encoding (PLACE) also uses two EPI acquisitions, where the difference between the two is a small increase in the area of the phase-encode preparatory gradient in order to add a linear phase difference between the two distorted images. The method is similar to PSF mapping techniques, though it is simplified and does not require a separate acquisition for measurement of the PSF. Post-processing of the image is rapid, and no phase unwrapping is required here [16].

3.1.3 Iterative Reconstruction

Iterative reconstruction is also very useful in distortion correction. The following forward model incorporates the measured field map in the reconstruction, but does not require that field map to be spatially smooth [7].

$$s(t_m) = \Phi(\vec{k}_{t_m}) \sum_{n=1}^{N} f(\vec{r}_n) e^{-i2\pi \vec{k}_{t_m} \vec{r}_n} e^{-i2\pi \Delta B(\vec{r}_n) t_m} \tag{3.2}$$

where $s(t_m)$ is the signal acquired at time point t_m, $\Phi(k)$ is the Fourier transform of the voxel indicator function, $\Delta B(r)$ is the field map, and the number of pixels in the image is N. Sutton's iterative method in [7] uses time-segmentation and the non-uniform FFT (nuFFT) to improve upon earlier implementations of iterative techniques, which results in fast computation for correction of distortion and blurring.

3.1.4 Correction Using PSF

Turning from field maps to the point spread function, PSF techniques are lauded for their compensation for both geometric distortion and signal loss. Unfortunately, a significant drawback is the extensive scan time required to measure the PSF for each voxel, requiring at least one reference scan for each line in the phase-encode direction for Robson's measurement.

This can be accounted for, as Zaitsev points out, by using a reduced field of view to take advantage of the sparseness of the PSF [17] or by adjusting the sampling pattern of the PSF acquisition [18]. To further speed up the PSF method, Zaitsev applies parallel imaging techniques to an optimized PSF method that is robust to high fields in [17].

3.1.5 During the Acquisition

From a hardware perspective, additional shims can also be used to account for the susceptibility-induced field inhomogeneity. Wilson, for example, uses an intra-oral shim that counteracts the field itself caused by susceptibility at the orbitofrontal region [19, 20]. Others suggest a mouth shim coil [21] or pyrolytic foam [22] to similarly confront the inhomogeneities themselves locally. However, these tools can worsen the uniformity of the field throughout the rest of the brain. The acquisition can also be altered to reduce the signal loss by manipulating the RF pulse [23, 24] or by changing the pulse sequence. The size of the voxels can be reduced [25, 26, 27].

3.1.6 Parallel Imaging

Finally, we look at how parallel imaging has impacted the field inhomogeneity problem. Put simply, faster imaging with less T2* decay and higher BWPP helps to avoid large distortions and signal loss: shorter time between lines means less phase accumulation and distortion in the phase-encode direction, and shorter acquisitions mean less signal loss. Methods that invoke parallel imaging [28, 29] inherently reflect this property by increasing the BWPP in the phase-encode direction and shortening acquisition time by reducing the number of lines acquired. Parallel imaging has significantly contributed to the fight against inhomogeneity effects and will continue to be incorporated

into field correction techniques.

CHAPTER 4

METHODS

4.1 Data Acquisition

4.1.1 Acquisition Sequence and Trajectories

All in vivo data was collected on a 3T Siemens Trio using a 12-channel head coil. All sequences were acquired using the following parameters: matrix size of 120x120; 25.6 cm field of view; 2.13x2.13x2 mm voxel size; 3 s TR; 27 axial slices each 2 mm thick; TE of 25 ms.

Three groups of functional images were collected to compare acquisition and reconstruction techniques: (1) standard single shot, single echo EPI with a GRAPPA factor of two reconstructed on the scanner with TE of 30 ms; (2) custom single shot, single echo EPI acquiring every other line anterior-posterior, then the opposite lines posterior-anterior (T(2,2,AP-PA), shown in Figure A.4); (3) custom one single shot, single echo EPI acquiring every fourth anterior-posterior, then every fourth line posterior-anterior (T(2,4,AP-PA), shown in Figure A.7). See Appendix A for an explanation of the k-space acquisition trajectories used.

Although the two subsets of lines are acquired within the same echo, they can be treated as two separate undersampled images with two different echo times.

4.1.2 Field Map and Sensitivity Map

In order to enable the measurement of the field map and mapping of receiver coil sensitivities for parallel image reconstruction, we acquired an asymmetric spin echo spiral acquisition. The acquisition has a spin echo of TE 20 ms, with asymmetric echoes offset at 1 ms. The spiral readout was sufficient for

a 120 matrix size. The first echo (the spin echo) was used to estimate the coil sensitivity maps by taking the coil images and dividing by the sum-of-squares image of all the coils. Then images were reconstructed from each echo using SENSE [28]. The difference in phase across echoes was divided by the difference in echo times in order to obtain the fieldmap, as shown in Equation 2.6.

4.2 Image Reconstruction

4.2.1 Formation of the Simulated Point Spread Function

The SPSF is derived using the k-space trajectory and timing vector alongside the measured field map. Using the field map (Figure 4.1.a), k-space trajectory (Figure 4.1.b), and acquisition timing to accurately estimate distortions in the acquisition, the MRI data for each point in image space (Figure 4.1.c) is simulated. Afterwards, each point in image space is reconstructed from the simulated data using a gridding technique (Figure 4.1.d), without knowledge of the field map, to form the $N^2 \times N^2$ SPSF matrix, $SPSF$.

For trajectories where interwoven lines are acquired in multiple subsets, the point spread functions are simulated and stacked (Figure 4.1.e). For example, for data is acquired in two subsets, $T1$ and $T2$, $SPSF = [SPSF_1; SPSF_2]$, where $SPSF_1$ and $SPSF_2$ are the corresponding SPSF matrices.

One important note about the SPSF reconstruction technique is that the field map is only used in simulating the MR data for the SPSF. Field correction is not included in the quick reconstruction for the SPSF, and the distorted images are also reconstructed without field correction. This way, the mismatch between the two distorted images with opposite phase-encode directions is maximized, leading to better distortion correction. This concept was verified in simulation, where the reconstructions using field-corrected SPSF and field-corrected data were compared to the uncorrected SPSF and uncorrected data.

4.2.2 Iterative Reconstruction

Coil sensitivity information (Figure 4.1.f) is combined with the $SPSF$ in order to form the system matrix A_{SPSF}. The distorted images corresponding to each subset of lines acquired are formed by gridded reconstruction from the acquired data, without any field correction (Figure 4.1.g). The undistorted image (Figure 4.1.h) can then be solved for in image space via conjugate gradient least squares by solving the following equation:

$$I_{distorted} = A_{SPSF} I_{undistorted} \tag{4.1}$$

where, in the case where lines are acquired in two subsets, $I_{distorted}$ are the two distorted images I_1 and I_2 stacked as $I_{distorted} = [I_1; I_2]$.

4.3 Simulation

Simulations were run in Matlab by simulating MRI data with field inhomogeneity from an image of a human brain, and the data was reconstructed as described above. For the error comparison, an image reconstructed from data simulated without field inhomogeneity and using a fully sampled k-space trajectory, T(1,1,AP) was used as the ground truth image.

4.4 Error Calculation

In order to objectively compare distortion correction in the images, we will use the norm root mean square error (NRMSE):

$$NRMSE = \sqrt{\frac{(|\hat{I}| - |I|)^T (|\hat{I}| - |I|)}{I^T I}} \tag{4.2}$$

where $\hat{I}$ is the corrected image and I is the true undistorted image. In simulation, I is the image derived from simulating fully-sampled data without the presence of field inhomogeneity and reconstructed using the coil sensitivity information in order to replicate the effect of processing on the image values.

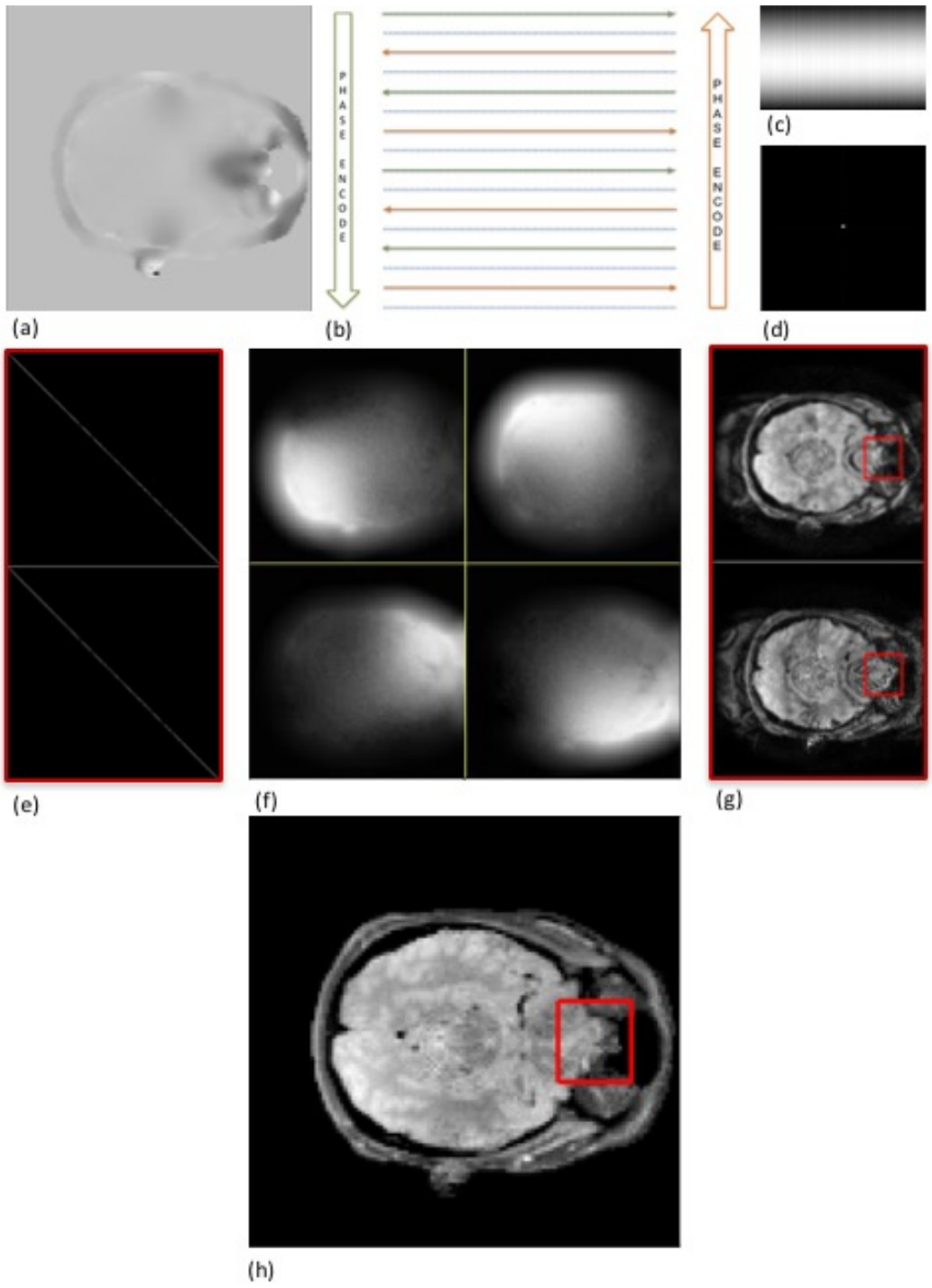

Figure 4.1: (a) Field map, (b) k-space trajectory, (c) simulated k-space data for a given point in image space, (d) simulated PSF for a given point in image space, (e) SPSF for each image, (f) coil sensitivity map, (g) distorted images, (h) iteratively corrected image

CHAPTER 5

RESULTS AND DISCUSSION

5.1 Field Map Analysis

Optimal acquisition trajectory may vary by slice based on field inhomogeneity in the brain. Large distortions can cause multiple blurred pixels to map to the same location, impeding distortion correction. Therefore, we can quantify the expected distortion by measuring the level of field inhomogeneity; this measure can be used to predict the success of SPSF correction for a given trajectory. The field inhomogeneity level can be determined quickly by analysis of the field map.

In order to determine the field inhomogeneity level, we first take the derivative of the field map (dFM), in order to determine which pixels will cause distortions larger than a pixel. We then assign a value to the inhomogeneity level by counting the percent of pixels in the dFM above the BWPP of the acquisition. The inhomogeneity levels for each slice and each acquisition trajectory for a particular field map are graphed in Figure 5.1. Note that T(1,1,*) is R=1, T(1,2,*) and T(2,2,*) fall into the R=2 category, and T(1,4,*) and T(2,4,*) fall into the R=4 category.

Since the acquired slices range from areas of high field inhomogeneity to low, we see a nice slope where the level is high lower in the brain and low in higher slices. As expected, the differences among the various trajectories are most pronounced in low slices where inhomogeneity is high.

The main idea behind increasing BWPP in order to increase tolerence of high field inhomogeneity is to contain the majority of the distortion of a given point to be less than a pixel in any direction. SPSF distortion correction falls apart when distortion exceeds a single pixel because distortions from multiple points overlap and are less separable. Thus, by choosing an acquisition to reduce distortion to a correctable range by increasing the BWPP, we optimize

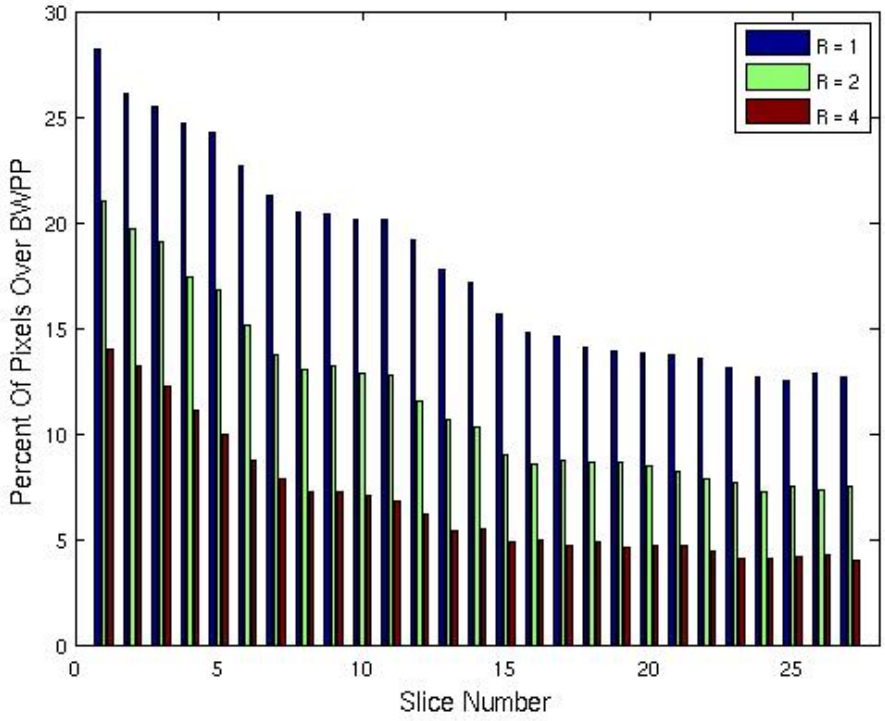

Figure 5.1: Percent of pixels of dFM that are over BWPP aacross 27 slices for fully sampled (blue), R=2 (green), R=4 (red) trajectories, where N=120, echospacing = 650 μs

distortion correction. In addition, by splitting the acquired lines into subsets with opposite phase encode directions, we increase separability of information about the distortion, which is in opposite directions for each subset of lines.

5.2 Simulation

5.2.1 Comparison of Acquisition Trajectories

For a description of the acquisition trajectories used in this work, see Appendix A. The notation used to identify the various trajectories is also defined in Appendix A.

Figure 5.2 shows the magnitude of the NRMSE across all slices for the various acquisition trajectories. Pairing this information with Figure 5.1, we see how the error changes as the field inhomogeneity level remains above or

falls below 15%. In low slices where there are large differences in inhomogeneity level and R=1 and R=2 trajectories are above 15%, there are large differences in error. However, in higher slices where inhomogeneity level is below 15% for all acquisitions, the difference in error is much less dramatic. As the level of field inhomogeneity levels off, error levels off in all cases.

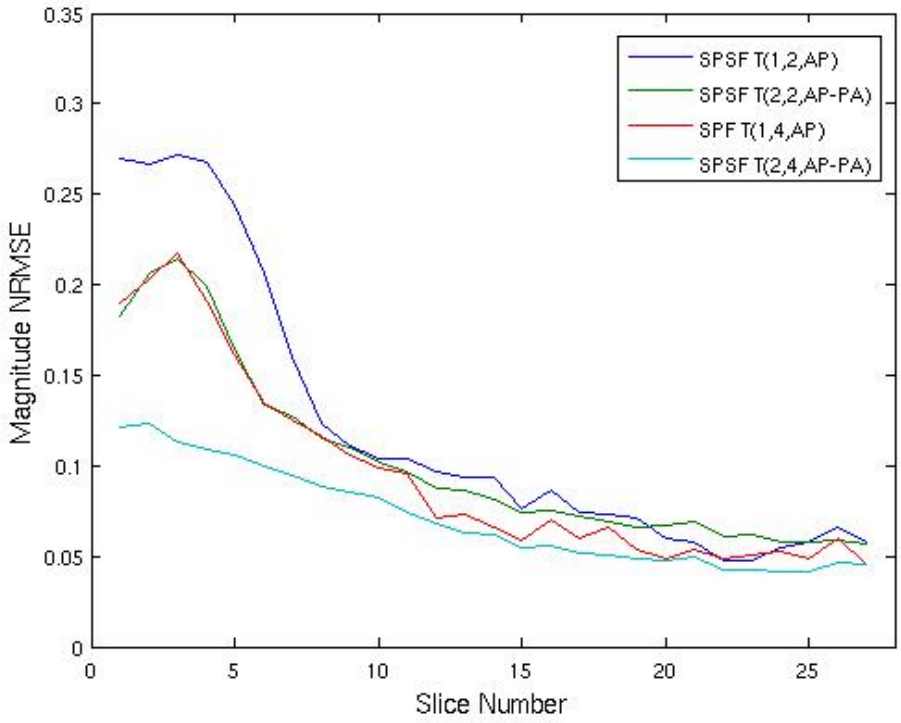

Figure 5.2: NRMSE across all slices using SPSF for distortion correction with various trajectories

Consistently, the inhomogeneity level shown in Figure 5.1 of an acquisition with a reduction factor of four remains below 15%, resulting in lower levels of distortion. For the highest inhomogeneity levels, acquisitions that undersample each subset by a factor of four yield optimal correction, as shown in Figure 5.2, as this acquisition has the highest BWPP. However, this benefit must be balanced by increased aliasing and slower convergence rate. In higher slices where the inhomogeneity levels are lower, aliasing artifacts play a greater role in image error.

We see T(1,2,AP) performing worst in low slices with high field inhomogeneity. Interestingly, the performance of the SPSF correction for T(1,4,AP) is on par with the T(2,2,AP-PA) acquisition. On one hand, T(2,2,AP-PA) is

preferable over T(1,2,AP) because it leverages the distortion mismatch due to opposite phase encode directions. On the other, T(1,4,AP) shrinks the distortion size to half of that of T(1,2,AP) and T(2,2,AP-PA), and SPSF is as robust here as T(2,2,AP-PA) with half as many samples. Figure 5.2 demonstrates that T(2,4,AP-PA) is optimal for distortion correction, as it combines the smaller distortions due to a reduction factor of 4 with the correction advantage of opposite phase encode directions. In higher slices with lower field inhomogeneity, the differences in error among the different acquisition trajectories become less pronounced.

Figure 5.3 compares SPSF reconstruction to the standard fast iterative reconstruction, which we will refer to as FastMR [7]. Clearly, acquisition trajectory impacts the robustness of FASTMR for distortion correction, but SPSF reconstruction is more robust overall for correction no matter which trajectory is used.

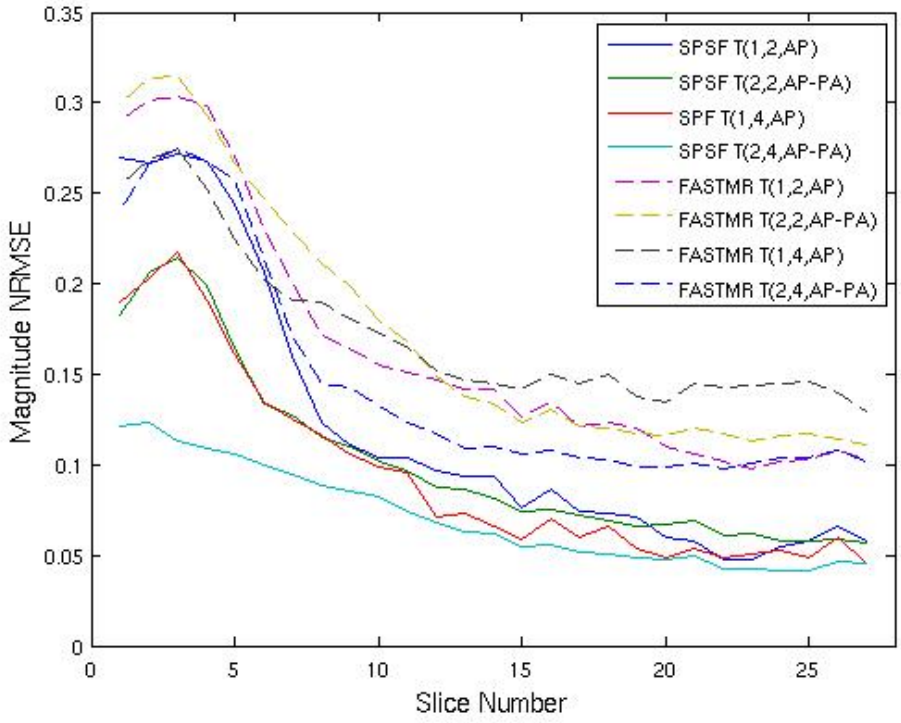

Figure 5.3: Error comparison of various acquisition trajectories using different reconstruction techniques

5.2.2 Convergence

Figure 5.4 compares the convergence rates of the various trajectories and SPSF vs. FastMR reconstructions. Note that the SPSF iterative reconstruction is much more stable; the FastMR reconstruction increases in error with many iterations. Comparing the trajectories reconstructed with SPSF, we observe that T(1,2,AP) converges faster than T(2,4,AP-PA), though they have the same overall number of samples.

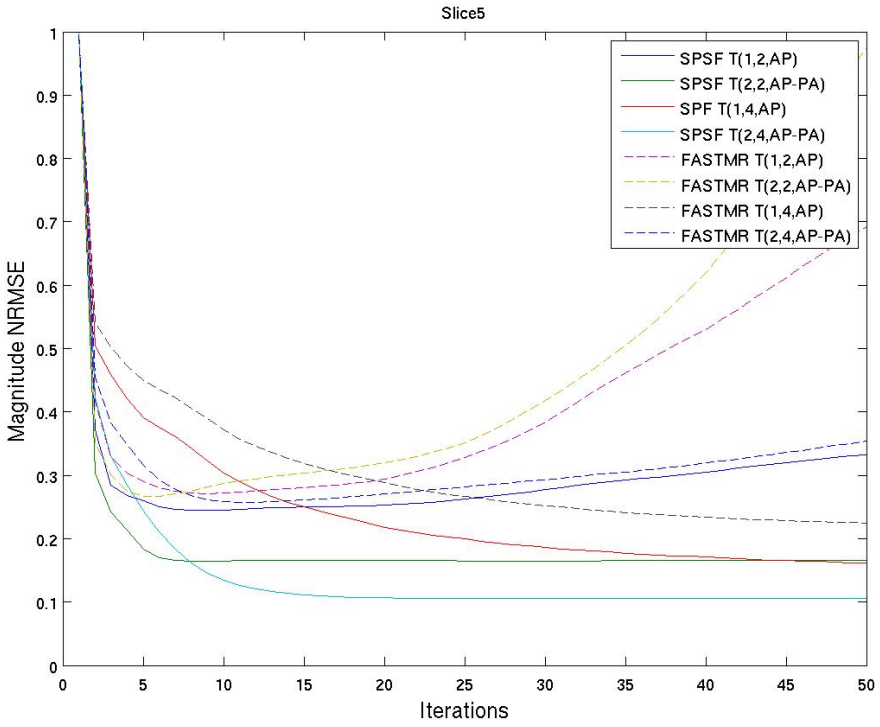

Figure 5.4: Convergence of SPSF vs. FASTMR iterative, low slice

5.2.3 Simulation Images

Figure 5.5 shows the field map used for a low slice (5) in simulation, which indicates large field inhomogeneity at this low slice. Figure 5.6 shows the undistorted image which is considered ground truth for the error measure. Figures 5.7 and 5.8 are the distorted images corresponding to T(1,4,AP) and T(1,4,PA) respectively, and the red boxes indicate the area of most significant distortion. Notice the opposite distortion directions, a result of the opposite

phase encode directions. Finally, Figure 5.9 is the SPSF corrected image, in which all distortion is corrected; again, the red box indicates the area corresponding to greated distortion in the original image.

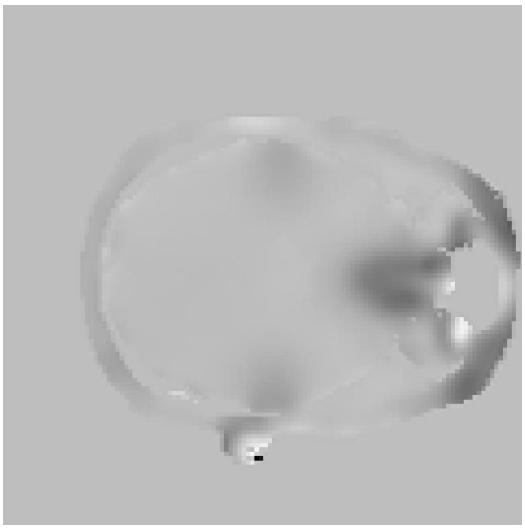

Figure 5.5: Field map, low slice

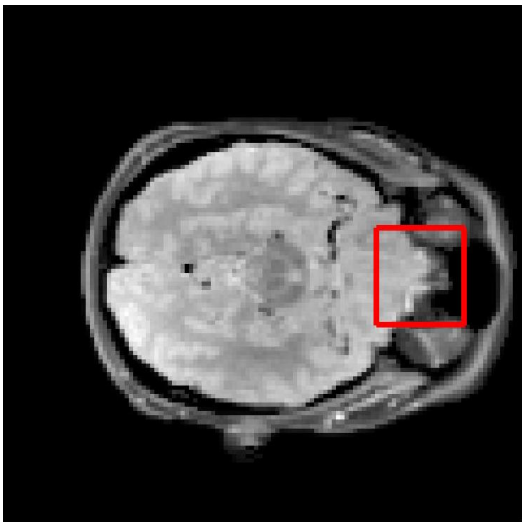

Figure 5.6: Simulation: Undistorted image, low slice

5.3 In Vivo

In vivo, the T(1,4,AP) and T(1,4,PA) images reconstruct seperately using the SPSF without alias. Figure 5.10 shows the distorted image, while Figure 5.11 shows the unaliased SPSF corrected image with much of the distortion

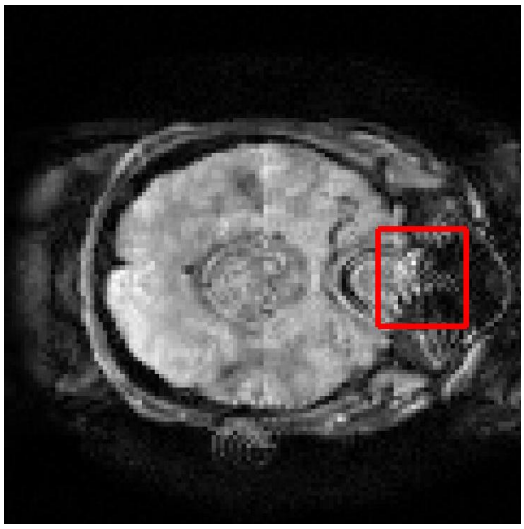

Figure 5.7: Simulation: Distorted image, T(1,4,AP), low slice

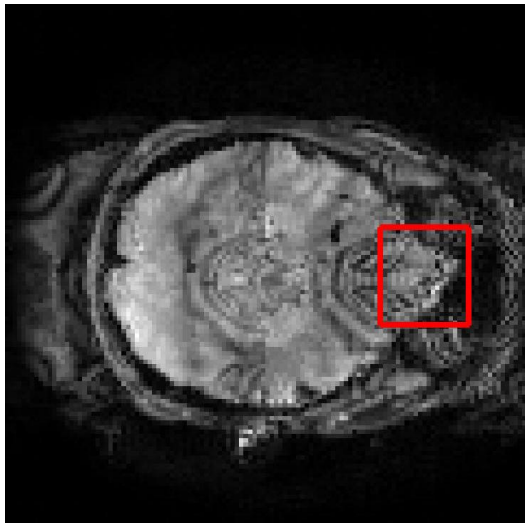

Figure 5.8: Simulation: Distorted Image, T(1,4,PA), low slice

corrected. The SPSF reconstruction out-performs the standard FastMR iterative method (Figure 5.12), which does not correct well for an undersampling factor of four using only four coils.

However, the combination of the two undersampled trajectories into T(1,4,AP-PA) exposes a flaw in our reconstruction and an omission in our data simulation. In Figure 5.13, we show the masked reconstruction of phantom data in order to clearly observe the quarter field of view aliasing pattern. We did not account for T_2* effects in our reconstruction, and this could likely be the cause of the artifact in T(2,4,AP-PA).

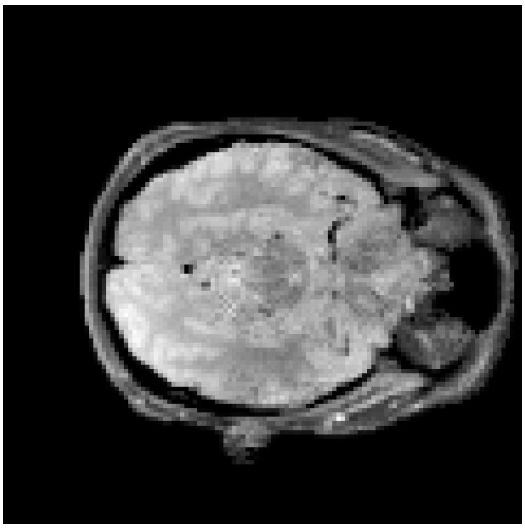

Figure 5.9: Simulation: SPSF Corrected Image, T(2,4,AP-PA), low slice

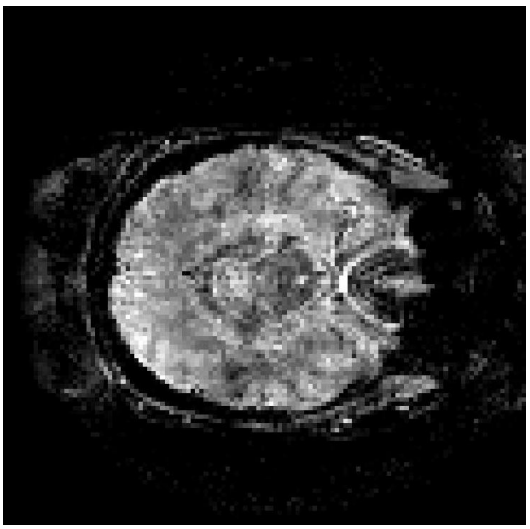

Figure 5.10: In vivo: Distorted image, T(1,4,AP), low slice

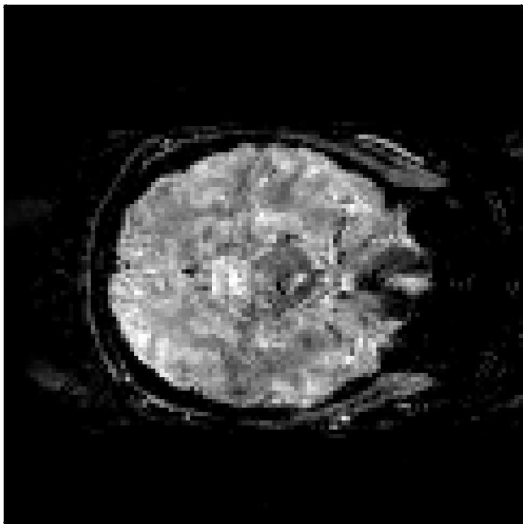

Figure 5.11: In vivo: SPSF corrected image, T(1,4,AP), low slice

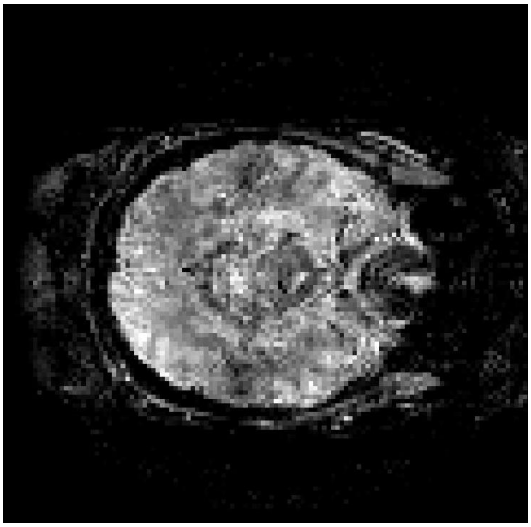

Figure 5.12: In vivo: FastMR corrected image, T(1,4,AP), low slice

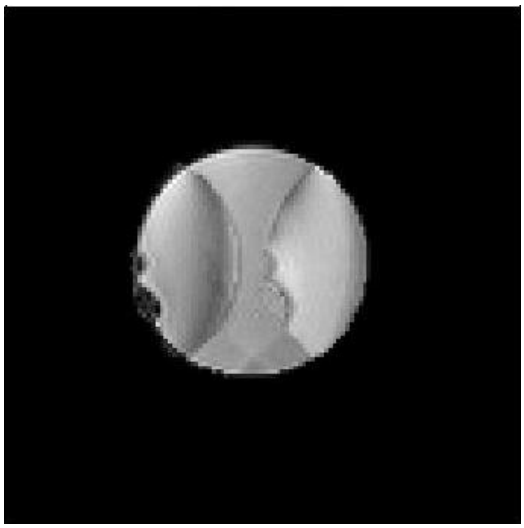

Figure 5.13: Phantom: SPSF Corrected Image, T(2,4,AP-PA)

CHAPTER 6

CONCLUSION

In conclusion, we have successfully simulated the PSF, rather than measuring it, and established that the SPSF is the most rigorous correction technique for distortion due to field inhomogeneity. Though the in vivo reconstruction of T(2,4,AP-PA) is obstructed by aliasing artifacts, we expect to correct for the artifacts in future work. The fact that the T(1,4,AP) and T(1,4,PA) images reconstruct without aliasing individually is promising and indicative that we can address the artifacts in T(2,4,AP-PA).

Though simulation found T(2,4,AP-PA) optimal in terms of error in all levels of field inhomogeneity, there may be some advantage to using the level of field inhomogeneity to select which trajectory is optimal for each slice. For example, there may be an advantage to T(1,2,AP) in some slices with low field inhomogeneity levels (where differences in error were small between different trajectories), such as faster convergence for the iterative algorithm or less error due to aliasing artifacts.

With the correction technique established and proven, the next step is to consider improving the time efficiency of the reconstruction and adapting the problem to a parallel implementation. Another important next step is to speed up the construction of the SPSF, which is slow and expensive in the current implementation. This step can be parallel. One possible implementation involves a library look-up of the approximate PSF for each voxel according to the value of the field map.

Condition number may be another tool for evaluating the advantages and disadvantages of each trajectory. The ideal point spread function is an identity matrix, meaning that information about a point in image space is restricted only to its own pixel and does not blur to other pixels. Since there is no blur to correct for, the margin for error is zero and convergence is immediate. This property is reflected in the condition number, which is equal to one for an identity matrix. Larger condition numbers could give us more informa-

tion about the properties of the SPSF. By calculating the condition number of the SPSF, we can get a sense of the margin of error and convergence rate of various trajectories. In future work, we will explore more carefully the role of the condition number in comparing acquisition trajectories.

APPENDIX A

DESCRIPTION OF ACQUSITION TRAJECTORIES

A.1 Naming Convention

A novel component of the data acquisition for the optimal SPSF is the k-space acquisition trajectory. Within each echo, we acquire the first set of k-space lines with twice the overall undersampling rate, then acquire the remaining lines with the phase-encode direction reversed. If N/R k-space lines are sampled for an NxN image with an over-all reduction factor of R, then (N/R)/2 evenly spaced k-space lines would be acquired from anterior to posterior, followed by (N/R)/2 evenly spaced lines acquired from posterior to anterior, with the two sets of lines intertwined.

We name here our different types of trajectories with the following naming convention: T(number of subsets within an echo, reduction factor within each subset, phase encode direction). One can calculate the total reduction factor of the trajectory by multiplying the subset reduction factor by the number of subsets.

For example, T(2,4,AP-PA) samples two subsets of k-space lines each with reduction factor of 4, with Anterior-Posterior as the phase encode direction of the first subset and Posterior-Anterior as the phase encode direction of the second subset.

A.2 Example Trajectories

The trajectories we will discuss in this work are the following:

T(1,1,AP) samples every k-space line from anterior to posterior, for a fully-sampled acquisition (Figure A.1).

T(1,2,AP) samples every other k-space line from anterior to posterior,

the standard acquisition for a reduction factor of two (see Figure A.2); its opposite, T(1,2,PA), is illustrated in Figure A.3.

T(2,2,AP-PA) samples every other k-space line from anterior to posterior, then reverses the phase encode direction, and samples every fourth line from posterior to anterior (Figure A.4).

T(1,4,AP) samples every fourth k-space line from anterior to posterior, the standard acquisition for a reduction factor of four (Figure A.5); its opposite, T(1,4,PA), is illustrated in Figure A.6.

T(2,4,AP-PA) samples every fourth k-space line from anterior to posterior, then reverses the phase encode direction, shifts up two lines, then samples every fourth line from posterior to anterior (Figure A.7).

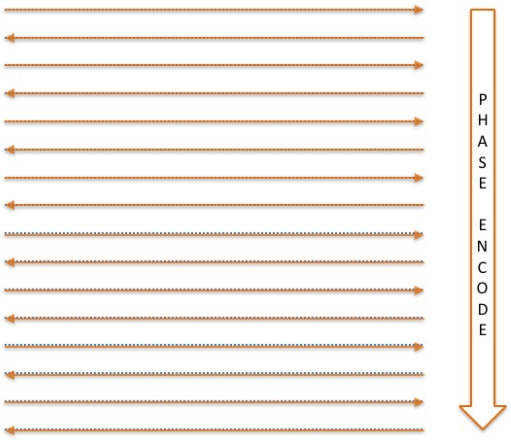

Figure A.1: T(1,1,AP)

Figure A.2: T(1,2,AP)

Figure A.3: T(1,2,PA)

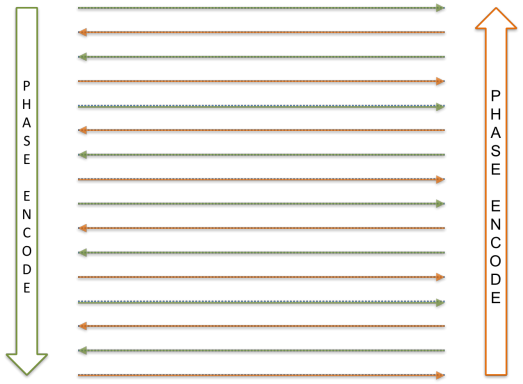

Figure A.4: T(2,2,AP-PA)

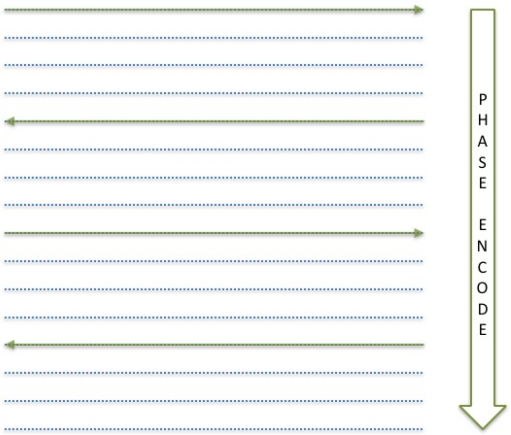

Figure A.5: T(1,4,AP)

Figure A.6: T(1,4,PA)

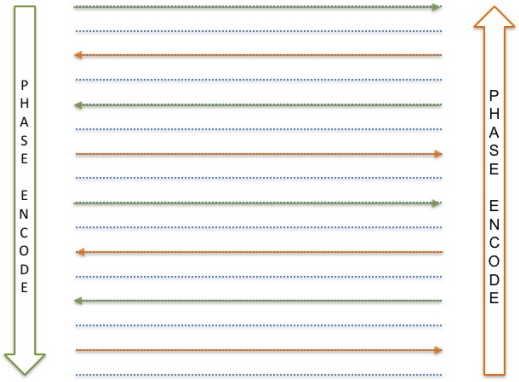

Figure A.7: T(2,4,AP-PA)

REFERENCES

[1] D. Holland, J. M. Kuperman, and A. M. Dale, "Efficient correction of inhomogeneous static magnetic field-induced distortion in echo planar imaging," *Neuroimage*, vol. 50, no. 1, pp. 175–83, 2010.

[2] B. Sutton, "Image reconstruction: Off-resonance effects and correction," *Intl Soc of Magnetic Resonance in Medicine*, 2012.

[3] P. Webb and A. Macovski, "Rapid, fully automatic, arbitrary-volume in vivo shimming," *Magn Reson Med*, vol. 20, no. 1, pp. 113–22, 1991.

[4] Z.-P. Liang and P. C. Lauterbur, *Principles of Magnetic Resonance Imaging: A Signal Processing Perspective*, ser. IEEE Press Series in Biomedical Engineering. Bellingham, Wash.: SPIE Optical Engineering Press, 2000.

[5] T. S. Sumanaweera, G. H. Glover, T. O. Binford, and J. R. Adler, "MR susceptibility misregistration correction," *IEEE Trans Med Imaging*, vol. 12, no. 2, pp. 251–9, 1993.

[6] M. D. Robson, J. C. Gore, and R. T. Constable, "Measurement of the point spread function in MRI using constant time imaging," *Magn Reson Med*, vol. 38, no. 5, pp. 733–40, 1997.

[7] B. P. Sutton, D. C. Noll, and J. A. Fessler, "Fast, iterative image reconstruction for MRI in the presence of field inhomogeneities," *IEEE Trans Med Imaging*, vol. 22, no. 2, pp. 178–88, 2003.

[8] H. R. Zeng and R. T. Constable, "Image distortion correction in EPI: Comparison of field mapping with point spread function mapping," *Magnetic Resonance in Medicine*, vol. 48, no. 1, pp. 137–146, 2002.

[9] B. Sutton, D. Noll, and J. Fessler, "Compensating for within-voxel susceptibility gradients in BOLD fMRI," *12th Soc. Magn. Reson. Med*, p. 349, 2004.

[10] D. C. Noll, C. H. Meyer, J. M. Pauly, D. G. Nishimura, and A. Macovski, "A homogeneity correction method for magnetic resonance imaging with time-varying gradients," *IEEE Trans Med Imaging*, vol. 10, no. 4, pp. 629–37, 1991.

[11] K. Sekihara, M. Kuroda, and H. Kohno, "Image restoration from non-uniform magnetic field influence for direct Fourier NMR imaging," *Phys Med Biol*, vol. 29, no. 1, pp. 15–24, 1984.

[12] P. Jezzard and S. Clare, "Sources of distortion in functional MRI data," *Hum Brain Mapp*, vol. 8, no. 2-3, pp. 80–5, 1999.

[13] P. J. Reber, E. C. Wong, R. B. Buxton, and L. R. Frank, "Correction of off resonance-related distortion in echo-planar imaging using EPI-based field maps," *Magn Reson Med*, vol. 39, no. 2, pp. 328–30, 1998.

[14] H. Chang and J. M. Fitzpatrick, "A technique for accurate magnetic resonance imaging in the presence of field inhomogeneities," *IEEE Trans Med Imaging*, vol. 11, no. 3, pp. 319–29, 1992.

[15] P. S. Morgan, R. W. Bowtell, D. J. McIntyre, and B. S. Worthington, "Correction of spatial distortion in epi due to inhomogeneous static magnetic fields using the reversed gradient method," *J Magn Reson Imaging*, vol. 19, no. 4, pp. 499–507, 2004.

[16] Q. S. Xiang and F. Q. Ye, "Correction for geometric distortion and N/2 ghosting in EPI by phase labeling for additional coordinate encoding (PLACE)," *Magn Reson Med*, vol. 57, no. 4, pp. 731–41, 2007.

[17] M. Zaitsev, J. Hennig, and O. Speck, "Point spread function mapping with parallel imaging techniques and high acceleration factors: fast, robust, and flexible method for echo-planar imaging distortion correction," *Magn Reson Med*, vol. 52, no. 5, pp. 1156–66, 2004.

[18] I. Dragonu, T. Lange, N. Baxan, J. Snyder, J. Hennig, and M. Zaitsev, "Accelerated point spread function mapping using signal modeling for accurate echo-planar imaging geometric distortion correction," *Magnetic Resonance in Medicine*, vol. 69, no. 6, pp. 1650–1656, 2013.

[19] J. L. Wilson, M. Jenkinson, and P. Jezzard, "Protocol to determine the optimal intraoral passive shim for minimisation of susceptibility artifact in human inferior frontal cortex," *Neuroimage*, vol. 19, no. 4, pp. 1802–11, 2003.

[20] J. L. Wilson and P. Jezzard, "Utilization of an intra-oral diamagnetic passive shim in functional MRI of the inferior frontal cortex," *Magn Reson Med*, vol. 50, no. 5, pp. 1089–94, 2003.

[21] J. J. Hsu and G. H. Glover, "Mitigation of susceptibility-induced signal loss in neuroimaging using localized shim coils," *Magn Reson Med*, vol. 53, no. 2, pp. 243–8, 2005.

[22] R. Shah, A. Chen, L. Li, B. Hargreaves, and S. Conolly, "An improved pyrolytic graphite foam for tissue susceptibility matching in MRI," *Proc. Intl. Soc. of Mag. Reson. Med. 15*, 2007.

[23] V. A. Stenger, F. E. Boada, and D. C. Noll, "Three-dimensional tailored RF pulses for the reduction of susceptibility artifacts in T2*-weighted functional MRI," *Magn Reson Med*, vol. 44, no. 4, pp. 525–31, 2000.

[24] V. A. Stenger, F. E. Boada, and D. C. Noll, "Multishot 3d slice-select tailored RF pulses for MRI," *Magn Reson Med*, vol. 48, no. 1, pp. 157–65, 2002.

[25] P. S. Bellgowan, P. A. Bandettini, P. van Gelderen, A. Martin, and J. Bodurka, "Improved bold detection in the medial temporal region using parallel imaging and voxel volume reduction," *Neuroimage*, vol. 29, no. 4, pp. 1244–51, 2006.

[26] K. D. Merboldt, J. Finsterbusch, and J. Frahm, "Reducing inhomogeneity artifacts in functional MRI of human brain activation-thin sections vs gradient compensation," *J Magn Reson*, vol. 145, no. 2, pp. 184–91, 2000.

[27] Y. Z. Wadghiri, G. Johnson, and D. H. Turnbull, "Sensitivity and peR-Formance time in MRI dephasing artifact reduction methods," *Magn Reson Med*, vol. 45, no. 3, pp. 470–6, 2001.

[28] K. P. Pruessmann, M. Weiger, M. B. Scheidegger, and P. Boesiger, "Sense: sensitivity encoding for fast MRI," *Magn Reson Med*, vol. 42, no. 5, pp. 952–62, 1999.

[29] M. A. Griswold, P. M. Jakob, R. M. Heidemann, M. Nittka, V. Jellus, J. Wang, B. Kiefer, and A. Haase, "Generalized autocalibrating partially parallel acquisitions (GRAPPA)," *Magn Reson Med*, vol. 47, no. 6, pp. 1202–10, 2002.